Journal of Alloys and Compounds 968 (2023) 172090

Contents lists available at ScienceDirect

Journal of Alloys and Compounds

journal homepage: www.elsevier.com/locate/jalcom

The role of TiO_2:SnO_2 heterojunction for partial oxidation of methane by photoelectrocatalytic process at room temperature

Ricardo Marques e Silva [a,b], Fernanda de Lourdes Souza [c], Eduardo Dias [a,c], Gelson Tiago dos Santos Tavares da Silva [d], Florymar Escalona Durán [a,e], Arjun Rego [b], Drew Higgins [b], Caue Ribeiro [a,*]

[a] Nanotechnology National Laboratory for Agriculture, Embrapa Instrumentation, São Carlos, São Paulo, Brazil
[b] Department of Chemical Engineering, McMaster University, Hamilton, Ontario, Canada
[c] Department of Chemistry and Molecular Physics, Institute of Chemistry of São Carlos, University of São Paulo, Brazil
[d] Interdisciplinary Laboratory of Electrochemistry and Ceramics, Department of Chemistry, Federal University of São Carlos, São Carlos, São Paulo, Brazil
[e] Department of Fuel and Hydrogen Cells, Nuclear and Energy Research Institute, São Paulo, São Paulo, Brazil

ARTICLE INFO

Keywords:
Methane oxidation
CH_4 oxidation
Photoelectrocatalysis
TiO_2:SnO_2 heterojunction

ABSTRACT

Partial Oxidation of Methane into hydrocarbons using photoelectrochemical routes is attractive from a sustainability point of view owing to the possibility of using renewable energy (i.e., solar illumination) to activate this stable molecule. However, the process demands the development of novel catalysts that can promote methane activation and oxidation in a controlled manner to increase energy conversion efficiency. Herein, we demonstrated that semiconductor heterostructures improved charge separation compared to the individual materials alone. A more effortless transfer between bands favors the separation of the electron-hole (e^-/h^+) pairs generated by the photoelectrocatalytic system and prevents them from recombining. This process produces reactive oxygens, essential to driving methane oxidation conversion of the C–H bond cleavage. TiO_2:SnO_2 semiconductor heterojunction catalysts in film shape were investigated for methane oxidation via a photoelectrocatalytic process. The methane oxidation reactions were carried out in an inflow and sealed electrochemical system for 1 h. Liquid-state nuclear magnetic resonance revealed methanol and acetic acid as the main liquid products, where the TiO_2:SnO_2 heterojunction exhibited better performance with values of 30 and 8 μmol. $cm^{-2}.h^{-1}$, respectively. Compared to their materials alone, the superior performance of the TiO_2:SnO_2 heterojunction is attributed to the formation of heterostructure type II that enables a more effortless transfer between bands, facilitating the separation of the generated e^-/h^+ pairs under UV-Vis irradiation. The outcomes achieved here will motivate further studies for developing semiconductor heterojunction structure catalysts in photoelectrocatalysis to partially oxidize methane into valuable chemicals.

1. Introduction

Methane, widely available as natural gas, is a versatile feedstock for chemical production [1]. However, due to its high stability and considerable carbon footprint, more environmentally friendly and economically efficient alternatives are required [2,3]. Partial methane oxidation reactions driven by photoelectrochemical processes have attracted interest as a promising alternative in this area of research. These reactions stand out for their capacity to use solar energy as a source of activation and external electrical energy to modulate the reactivity of the reaction and the selectivity of the products [4].

Currently, most of the research in the electrochemical activation of methane has used metal and metal alloy catalysts, such as Au, Pt, and Pt-Rh [3,5,6]; however, these catalysts tend to favour the complete oxidation of methane to CO_2 as opposed to partial oxidation into value-added chemicals/fuels. Metal oxide semiconducting materials are being used as a more controlled method to solve this problem because they may modify the reaction rate. The reactive species produced may vary depending on factors like composition, shape, and bandgap, which could alter the reaction's route and product selectivity. The reaction mechanism involving metal oxide semiconducting materials involves the generated electron-hole (e^-/h^+) pairs when excited from an

* Corresponding author.
E-mail address: caue.ribeiro@embrapa.br (C. Ribeiro).

https://doi.org/10.1016/j.jallcom.2023.172090
Received 7 June 2023; Received in revised form 7 September 2023; Accepted 7 September 2023
Available online 9 September 2023

illuminated light source. These generated e^-/h^+ on the surface of the semiconductor lead to the formation of reactive species, e.g., hydroxyl radicals (•OH) and superoxide anion radicals ($O_2^{\bullet -}$), which can be more selective in the formation of products, depending on the oxidation state of the metal and the chemical interactions involved. Although the thermodynamic barrier for C−H bond activation is high, oxidative sites such as metal centers, the •OH, and $O_2^{\bullet -}$ species can provide the necessary energy to overcome it and form a new bond [7,8].

Among the metal oxide semiconducting materials, TiO_2 anatase has been investigated as a photoelectrocatalyst for methane oxidation [2,9]; however, its relatively low surface area limits the availability of active sites for the reaction, reducing its activity, and its relatively high recombination rate; where photogenerated e^-/h^+ pairs tendency to recombine rather than participate in the desired reaction, limiting its efficiency. In this sense, a semiconductor heterojunction can overcome these issues since the interface formed between two different semiconductor materials with different electronic properties can improve their properties, surface area (increasing), and recombination rate (decreasing − when a heterojunction is formed, the e^-/h^+ diffuse across the junction, creating a depletion region with a built-in electric field that aids in charge separation; by draining the photogenerated electrons from one phase to the other phase in contact, it prevents the reverse diffusion back across the junction) [10].

In particular, the TiO_2:SnO_2 heterostructure is worth studying because (i) it presents sufficient oxidative potential to oxidize the water molecules due to the valence band maximum of both TiO_2 and SnO_2 being lower than the potential of •OH/OH^- (+2.59 V versus NHE) and the conduction band minimum of TiO_2 being higher than the potential of $O_2/\bullet O_2^-$ (−0.16 V versus NHE)[11], (ii) SnO_2-rutile possess higher surface area than TiO_2-anatase, making the TiO_2:SnO_2 heterojunction activity higher, and (iii) the TiO_2:SnO_2 heterojunction is easily synthesized since both are crystallized in the same crystallographic group, i.e., SnO_2-rutile and TiO_2-anatase phases share standard crystalline planes. The self-organization of TiO_2:SnO_2 heterostructures using preformed particles via a hydrothermal method is possible through the Oriented Attachment growth mechanism [12,13]. Although there is evidence related to the effectiveness of TiO_2:SnO_2 to conduct advanced oxidation processes (AOP), the literature focuses on complete oxidation of target molecules (e.g., dyes, pesticides, etc) [14]. Studies about the performance of these catalysts in the partial oxidation processes are incipient, leading that the knowledge about how to control the extension of reactions is unclear. Especially on the case of methane partial oxidation, the capacity of the catalysts to activate the molecule is the main unaddressed challenge. The understanding of the process as a whole is complex, including the description of how the particles' alignment influences the electronic levels positions (i.e., holes and electrons), and how the oxidizing species are formed.

Therefore, in this study we produced TiO_2:SnO_2 heterostructure looking for the benefits of the charge migration promoted by photoelectrocatalytic process for the partial methane oxidation. Using an external potential can control the rate and extent of oxidation, promoting desired intermediate products, such as methanol (CH_3OH) and acetic acid (CH_3COOH). Thin films of TiO_2:SnO_2 were prepared by dispersing the catalysts in water suspensions and spray-coating them on Fluorine-doped Tin Oxide (FTO) substrate. Since we suppose the electrons will be concentrated in the SnO_2 side of the heterostructure, the choice of FTO attends to the energy-level alignment to promote fast and easy electron capture (to the electrochemical circuit). The prepared photoelectrodes (i.e., TiO_2:SnO_2 heterojunction, TiO_2-anatase, and SnO_2-rutile) were evaluated for their capability to oxidize methane using an inflow and sealed electrochemical system, excited by three different sources (i.e., electron, photon, and photoelectron). As a result, as-synthesized TiO_2:SnO_2 heterostructure electrodes excited by a photoelectron source exhibited superior performance for methanol (30 μmol.cm^{-2}.h^{-1}) and acetic acid (8 μmol.cm^{-2}.h^{-1}) production when compared to their materials alone (i.e., TiO_2-anatase and SnO_2-rutile). These results motivate new photoelectrocatalyst experiments using heterojunction catalysts to partially oxidize methane into value-added chemicals.

2. Experimental

2.1. Chemicals

All chemicals, including anhydrous titanium(IV) oxide ($TiO_2 \geq$ 99.99%), tin(II) chloride ($SnCl_2$), anhydrous sodium carbonate (Na_2CO_3), and anhydrous alcohol (99.5%) were analytical grade and used as received from Sigma Aldrich. Type I ultrapure water (Millipore Milli-Q system, resistivity of 18.2 MΩ cm at 25 ºC) was used to prepare all solutions. Nitrogen (N_2) and methane (CH_4) gas (99.99%, purity) were purchased from White Martins Inc. (Brazil). D521 Nafion® alcohol-based dispersion 5 wt% from Fuel Cell Store was employed as binding for the electrode deposition. Fluorine doped tin oxide coated glass (FTO – 2.2 mm) with surface resistivity ~7 Ω sq^{-1} were purchased from Sigma Aldrich.

2.2. Electrode preparation

Three different catalysts were prepared before spraying on the FTO substrate: (i) containing commercial TiO_2-anatase particles, (ii) containing as-synthesized SnO_2-rutile, which were synthesized at room temperature and annealed via hydrothermal at 200 °C for 240 min, according to Torres et al., 2020 [15], and (iii) containing a blend (75–25 wt%) as-synthesized TiO_2:SnO_2 heterojunction, which was synthesized by adding commercial TiO_2-anatase, SnO_2 precursor, and type I ultrapure water to the stainless steel vessel, kept under stirring at room temperature (25 °C) for 20 min and taken it to the hydrothermal heating at 200 °C for 240 min, as reported by Mendonça et at. 2014 [13]. The films were prepared by spray-coating on FTO (dimensions 2.5 ×2 cm) substrates, which were cleaned before coating in multiple steps (i) using type I ultrapure water and Extran® soap under sonicating for 5 min, (ii) ethanol under sonicating for 5 min, (iii) acetone under sonicating for 5 min, (iv) type I ultrapure water under sonicating for 5 min to remove impurities/contaminants, and (v) dried in N_2 flux. For all depositions, a catalyst slurry was prepared by mixing 25 mg of catalyst in 25 mL of isopropanol and 0.25 mL Nafion® for 20 min using a mortar and pestle, and the slurry was then dispersed in 100 mL of isopropanol under sonication for 30 min. The semiconductor suspensions were sprayed on the FTO over a heating plate at 60 ºC to increase the solvent evaporation rate.

2.3. Characterization

The crystalline structure of commercial TiO_2-anatase, as-synthesized SnO_2, and as-synthesized TiO_2:SnO_2 powders were analyzed by X-Ray Diffraction (XRD − Shimadzu XRD-6000 diffractometer model) using a Cu Kα source (λ = 1.5418 Å) operated at 30 kV and 30 mA. The data were acquired at diffraction angles ranging from 10° to 90° with a scanning velocity of 2° min^{-1}. Raman spectra were recorded (Raman - Horiba LabRam HR Evolution) using a laser excitation wavelength of 532 nm from 100 to 1000 cm^{-1}. A scanning transmission electron microscope (STEM − FEI Tecnai G2 F20) equipped with high-resolution images (HRTEM) and Energy-dispersive X-rays (EDX) was used to determine morphologies, crystalline plans, and chemical compositions of the samples. A colloidal alcoholic suspension of each sample was dispersed and directly dropped onto a carbon-coated copper grid and allowed to dry before being taken to the microscope. The nitrogen adsorption−desorption isotherms and the Brunauer−Emmett−Teller (BET) specific surface areas were measured using a Micromeritics ASAP 2020 instrument operating at − 196 °C. The Tauc method [16] was applied to calculate the indirect bandgap energy of each sample using the diffuse reflection spectrum (DRS, Shimadzu UV-2600

spectrophotometer). The photoluminescence (PL) was recorded using an excitation laser source with a wavelength at 355 nm under a constant power of 5 mW and concentrated upon a 200 μm spot. The luminescence signal was dispersed by a 19.3 cm spectrometer (Andor/Kymera) and detected by a Si charge-coupled device (Andor/Idus BU2). 1 H nuclear magnetic resonance (NMR – Bruker, model Bruker Ascend™ 600 MHz) operating at 25 °C was used to identify and quantify liquid products. Aliquots of 540 μL of each sample were mixed into a solution with 60 μL of D20, 50 mM of standard dimethyl sulfoxide (DMSO), and 0.21 mM of reference 3-(trimethylsilyl)propionic-2,2,3,3-d4 acid sodium salt (TSPd4). The WET procedure suppressed the water peak, and the raw NMR data were investigated using the MestReNova software.

2.4. Flow cell configuration

The experimental setup for partial oxidation of methane was designed using a customized filter-press photoelectrochemical reactor with an inflow and sealed system (Fig. S1). The lab-scale system consists of i) anolyte and catholyte jacketed glass tanks with a capacity of 100 mL coupled to a thermostatic bath; ii) peristaltic pumps to recirculate the fluid through the photoelectroreactor; iii) a 100 W halogen lamp; and iv) a double compartment photoelectrochemical flow cell. The cathode and anode chambers of the photoelectrochemical reactor were made from Teflon and polyacetal, respectively. Both compartments are separated by two rubber seals (thickness ca. 4.8 mm) and a cation exchange membrane, Nafion 117. SAE 304 stainless steel was used as the counter electrode, while the as-prepared electrodes were employed as the working electrode. The electrodes have an effective active area of 5 cm^2. The catalyst loading was 3.0 ± 2 $mg.cm^{-2}$. An Ag/AgCl 3.0 M KCl reference electrode was used and placed near the working electrode in the cathodic compartment. All the fluid connections were located at the side plate of the reactor. Lastly, 1 mm thick Viton® sheets and gaskets were used to ensure a leak-free operation. The photoelectrochemical reactor was sealed by hand using M6 bolts at 4 Nm. Each experiment was conducted on fresh film and electrolyte, and different types of excitations were applied on the electrodes (i.e., electro reactions were done only over the applied potential, photon reactions were done only over the UV-Vis irradiation, and photoelectron reactions were done with the applied potential and UV-Vis irradiation). The experimental preparation process was the same for all reactions, except for the previously mentioned excitation source. The cathodic and anodic chambers contain 3.2 mL each, but the reactional volume of the reservoirs was 100 mL of 0.5 M Na_2CO_3 electrolyte of pH 12. The catholyte was purged with a constant flow (30 mL min^{-1}) of N_2 for 20 min, followed by saturation with methane gas (30 mL min^{-1}) for 30 min. Chronoamperometric measurements at 1.3 V, controlled with an Autolab potentiostat (Multi Autolab/M204), for electron reactions, a 100 W halogen lamp source for photon reactions, and both chronoamperometric measurements at 1.3 V and a 100 W halogen lamp source were applied for photoelectron reactions. Essays were performed in a discontinuous mode, and the recirculation through the reservoir and the photoelectrochemical reactor was kept at a 14 mL min^{-1} flow rate.

3. Results and discussion

X-ray diffraction (XRD) was carried out to investigate the

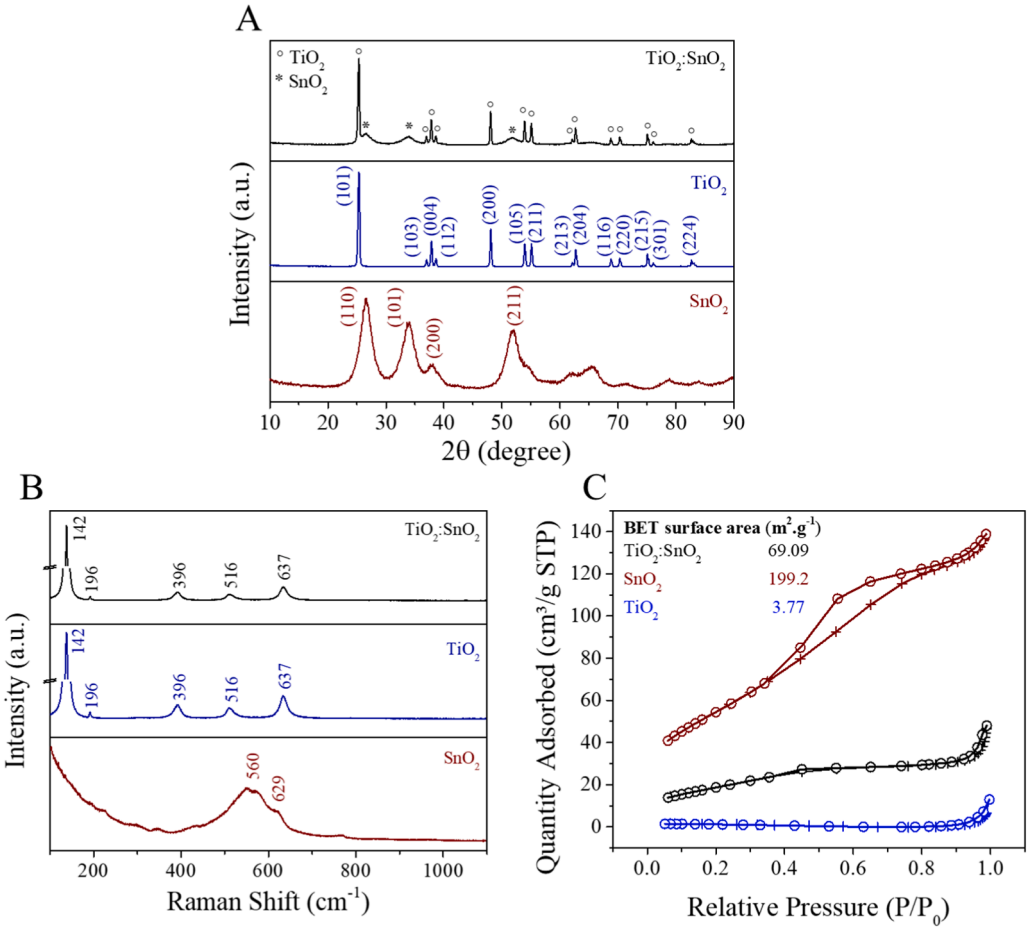

Fig. 1. (A) XRD patterns, (B) Raman spectra, and (C) Nitrogen adsorption-desorption isotherm and surface area (inset) for the as-synthesized TiO_2:SnO_2 heterostructure, commercial TiO_2-anatase, and as-synthesized SnO_2-rutile samples.

crystallographic structure of the as-synthesized TiO_2:SnO_2 heterostructure, commercial TiO_2-anatase, and as-synthesized SnO_2-rutile samples, as shown in Fig. 1(A). Regarding commercial TiO_2, all diffraction peaks are indexed to the anatase phase of TiO_2 with a tetragonal crystal structure and a lattice constant of $a = 0.3784$ nm and $c = 0.9515$ nm, according to the Joint Committee on Powder Diffraction Standards (JCPDS) card No. 21–1272. For the as-synthesized SnO_2, the main diffraction peaks can be indexed to the rutile phase of SnO_2 with a tetragonal crystal structure (JCPDS card No. 41–1445), which corresponds to the (*hkl*) planes of (110), (101), (200), and (211) with a lattice constant of $a = 0.473$ nm and $c = 0.3185$ nm. For the as-synthesized TiO_2:SnO_2 heterostructure, diffraction peaks characteristic of both anatase TiO_2 and rutile SnO_2 phases were identified, indicating integration of the different phases and a potentially successful synthesis.

Raman spectroscopy was performed to investigate the short-range order of the different samples, as shown in Fig. 1(B). Regarding commercial TiO_2, the Raman bands located at 142, 196, 396, 516, and 637 cm^{-1} are attributed to the anatase phase of TiO_2. The bands at 142, 196, and 637 cm^{-1} are assigned to the E_g mode, the band at 396 cm^{-1} corresponds to the B_{1g} mode, and the band at 516 cm^{-1} is assigned to the A_{1g} mode [17]. To the as-synthesized SnO_2, the peak at 560 cm^{-1} can be assigned to the Sn−O surface vibrations, and the peak at 629 cm^{-1} can be assigned to the A_{1g} mode of SnO_2 [18]. To the as-synthesized TiO_2:SnO_2 heterostructure, there was no signature for the SnO_2 vibration modes; however, the band intensities have decreased when compared to the pure TiO_2, indicating that introducing SnO_2 on the TiO_2 surface will not change the crystal phase of TiO_2 [19]. It was not possible to identify the Raman shifts referring to the rutile phase of the SnO_2 due to the peaks overlapping since the peak at 629 cm^{-1} is close to the anatase phase of the TiO_2 peak at 637 cm^{-1} which is more intense.

To analyze the Physical adsorption behavior and the specific surface areas, the BET technique was applied, and the results are displayed in Fig. 1(C). According to the IUPAC Technical Report [20], pure TiO_2 presents reversible Type I(a) isotherms, possibly due to their pore size width of ~8 nm and relatively small external surface. The as-synthesized SnO_2 presents the Type IV isotherms given by its mesoporous adsorbents with pores wider than ~4 nm and a surface area of 199.2 $m^2.g^{-1}$. The as-synthesized TiO_2:SnO_2 heterostructure shows the reversible Type II isotherms given by the physisorption macroporous adsorbents. An increased specific surface area of TiO_2:SnO_2 (69.09 $m^2.g^{-1}$) was achieved when compared to the commercial TiO_2-anatase (3.77 $m^2.g^{-1}$).

The structure and morphology of the as-synthesized TiO_2:SnO_2 heterostructure (Fig. 2), commercial TiO_2-anatase (Fig. S2A), and as-synthesized SnO_2-rutile (Fig. S2B) were imaged via electron microscopy. Fig. 2A represents the SEM micrographs of as-synthesized TiO_2:SnO_2 heterostructure, showing particles with a nearly-spherical shape and an average size of 139 nm (particle size distribution Fig. S2D) covered with small particles, attributed to SnO_2. Commercial TiO_2-anatase particles remained with their structure intact, and there were no changes of shape or phase even after the heat treatment during SnO_2

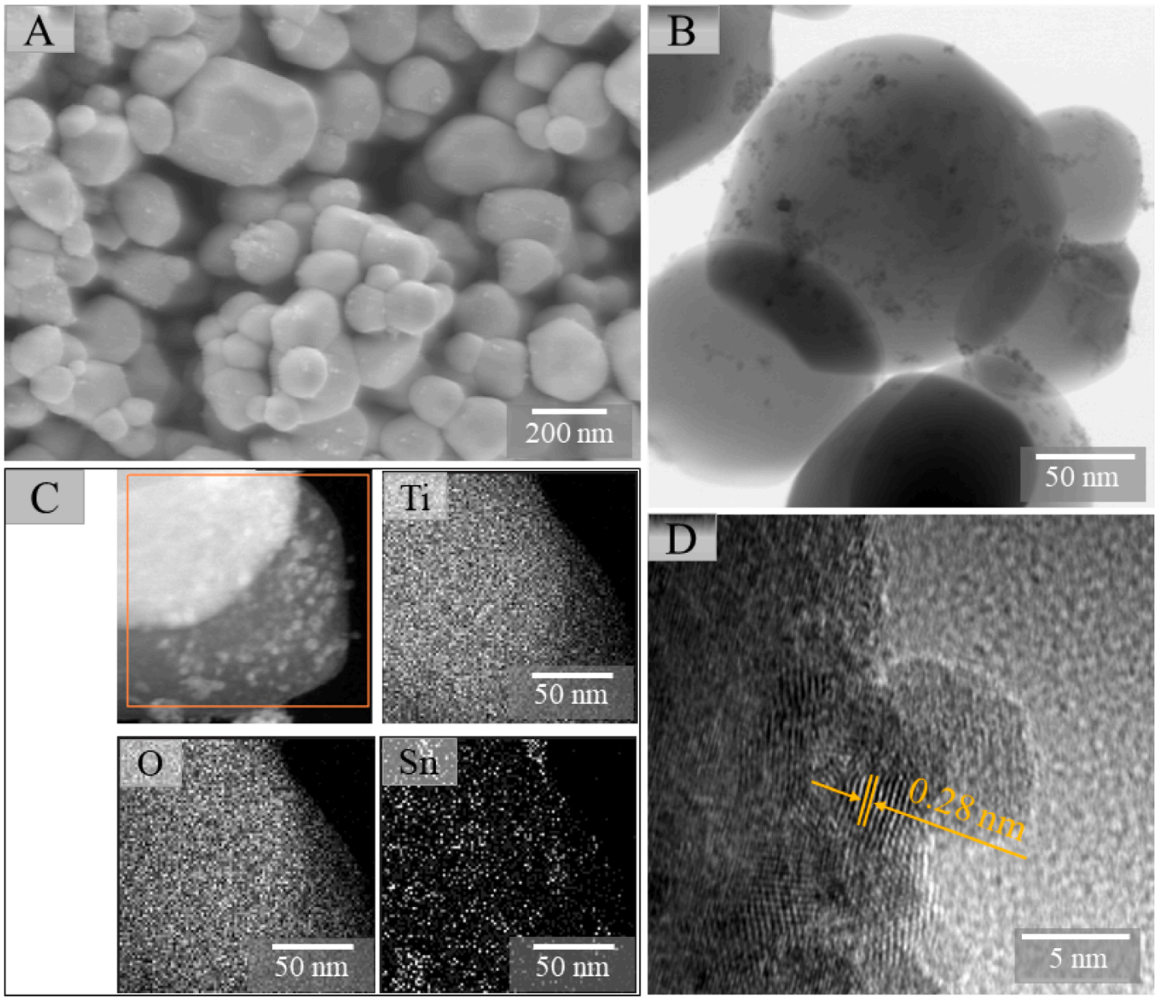

Fig. 2. Electron micrographs of the as-synthesized TiO_2:SnO_2 heterostructure, (A) SEM image, (B) TEM image, (C) TEM-EDX, (D) HRTEM image (zoom of the SnO_2 nanoparticles over the TiO_2 showed in Fig. 2B).

nanoparticle growth, indicating good structural stability and a tight interfacial contact, which can benefit in enhancing the reaction kinetics [19]. Fig. 2B shows a TEM image of the as-synthesized TiO_2:SnO_2 heterostructure and Fig. 2D (zoom of the SnO_2 nanoparticles over the TiO_2) that reveals small crystalline SnO_2 nanoparticles located on the smooth surface of the TiO_2 particle. Fig. 2C shows the TEM-EDX analysis that identifies the presence of uniformly distributed Sn on the Ti particles. Fig. 2D shows the high-resolution TEM image of the as-synthesized TiO_2:SnO_2 heterostructure, revealing the presence of partially facetted and chained crystalline nanoparticles, forming three-dimensional aggregates. The crystallographic plane of SnO_2 shows the adjacent interplanar distance of 0.28 nm in relation to plane 110. Moreover, the coalescence between SnO_2 nanoparticles is highlighted. These results indicated that the as-synthesized TiO_2:SnO_2 heterostructure had been successful. It is important to state that despite observed interfaces between the particles, heterojunction formation cannot be confirmed only by TEM analysis since a heterojunction is elucidated by the possibility of charge migration between the different semiconductors forming, thus a heterostructure.

Ultraviolet-visible (UV–vis) spectroscopy of the as-synthesized TiO_2:SnO_2 heterostructure, commercial TiO_2-anatase, and as-synthesized SnO_2-rutile are shown in Fig. 3(A). The Tauc equation applied to the UV–vis diffuse reflectance was used to measure the bandgap energy of each sample. The experimental results indicated that the commercial TiO_2-anatase and as-synthesized SnO_2-rutile exhibited strong photoabsorption below 400 nm (i.e., in the UV range) from the indirect transitions. However, the energy band of as-synthesized SnO_2-rutile (3.74 eV) is higher than commercial TiO_2-anatase (3.2 eV). The lower bandgap value presented by the commercial TiO_2-anatase suggests an easier electron transition between the valence and conduction bands, which qualifies its use as a support for a photocatalytic process [21]. The addition of Sn did not shift the bandgap energy of TiO_2; that is, there was no doping of Sn into the TiO_2 structure. Instead, the SnO_2 particles were effectively grown onto the TiO_2 surface, producing a particle with single electron levels that allow sharing of photogenerated electrons and holes in catalytic processes [22].

The photoluminescence (PL) emission of the as-synthesized TiO_2:SnO_2 heterostructure, commercial TiO_2-anatase, and as-synthesized SnO_2-rutile was recorded in the 360–1000 nm range with an excitation wavelength of 355 nm, as displayed in Fig. 3(B). PL spectra for all materials showed a weak UV light emission peak at ~365 nm, which corresponds to the internal transition of the electrons from the conduction band to the valence band [23]. In addition, the as-prepared polycrystalline oxides exhibited blue emission (460–480 nm) attributed to electronic transition mediated by defect levels (oxygen vacancies) in the bandgap. Commercial TiO_2-anatase exhibited a strong emission of ~477 nm attributed to charge transfer from Ti^{3+} to an oxygen anion in a TiO_6 octahedron [24]. Similarly, as-synthesized SnO_2-rutile exhibited an emission at ~473 nm associated with electronic transitions from the Sn^{4+} ion to oxygen. However, it also showed a broad band with a maximum of ~621 nm, which can be attributed to surface hydroxyl groups [15,25]. Regarding the as-synthesized TiO_2:SnO_2 heterostructure, the main emission is found in the same region of the commercial TiO_2-anatase (~477 nm), indicating exceptional contribution of the electronic transition from the oxygen vacancies in the TiO_2 structure. However, the emission intensity of the as-synthesized TiO_2:SnO_2 heterostructure is shown to be lower than that of commercial TiO_2-anatase suggesting that the anchoring of SnO_2 nanoparticles on the surface of TiO_2 particles facilitates electronic transitions, making it more effective in controlling and reducing the recombination of e^-/h^+ pair carriers [25], indicating that heterojunction between TiO_2 and SnO_2 was successfully achieved.

Production of liquid chemicals from partial oxidation of methane of different electrodes (i.e., as-synthesized SnO_2-rutile, commercial TiO_2-anatase, and as-synthesized TiO_2:SnO_2 heterostructure) after 1 h of reaction are shown in Fig. 4. All electrodes were subjected to the same experimental conditions, with the exception of the different sources of excitement (i.e., photon, electron, and photoelectron). The as-synthesized TiO_2:SnO_2 heterostructure samples under photoelectron excitation showed superior performance among the studied catalysts. Liquid-state NMR revealed methanol and acetic acid were the main liquid products for all reaction configurations (photon, electron, and photoelectron sources), indicating good selectivity. A pre-reaction was made under the same experimental reaction standards; that is, the photoelectrochemical reactor was assembled with all apparatus, gas flow, and fresh electrolyte (details in flow cell configuration section), but with no electrode or employment of potential and light irradiation. A minor amount of methanol was identified in this pre-reaction, and this amount was subtracted from the values of all reactions.

All studied catalysts showed distinct behavior when induced by the different sources of excitement and, therefore, different total productions. When just photoexcited, the as-synthesized SnO_2-rutile electrodes presented no methanol or acetic acid production. On the other hand, commercial TiO_2-anatase and as-synthesized TiO_2:SnO_2 heterojunction electrodes exhibited similar production, indicating that the presence of SnO_2-rutile did not influence the behavior of the as-synthesized TiO_2:SnO_2 heterojunction. This finding suggests that the observed behavior aligns with the TiO_2-anatase attributes as a catalyst since it possesses a lower bandgap and higher energy positions of the conduction band (−0.5 V vs. NHE) than SnO_2-rutile (0.5 V vs. NHE), which is adequate to water splitting – it is essential to form a hydroxyl radical (•OH) that reacts with methane (CH_4) to produce a methyl

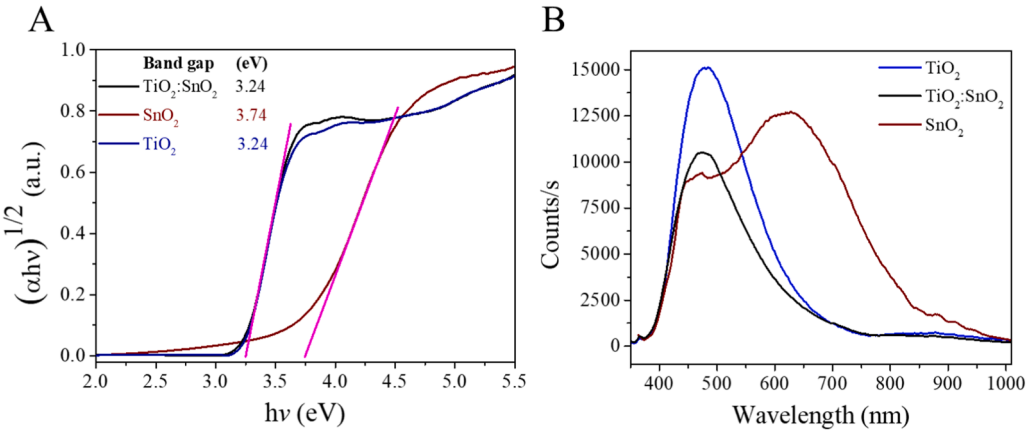

Fig. 3. (A) UV–vis diffuse reflectance spectra and Tauc plot (indirect bandgap value) and (B) photoluminescence (PL) spectra of the as-synthesized TiO_2:SnO_2 heterostructure, commercial TiO_2-anatase, and as-synthesized SnO_2-rutile samples.

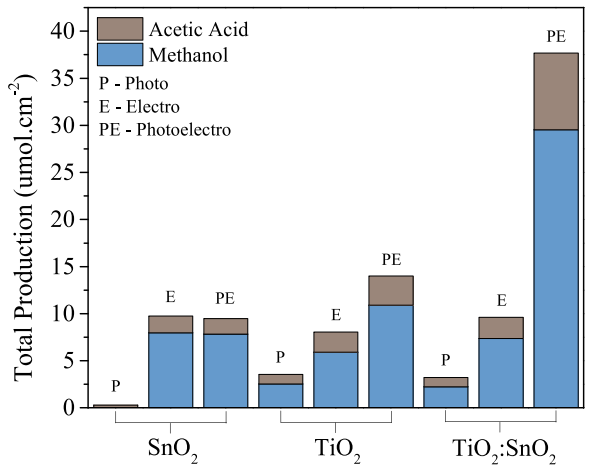

Fig. 4. Total production of liquid chemicals from partial oxidation of methane of different electrodes consisting of as-synthesized SnO_2-rutile, commercial TiO_2-anatase, and as-synthesized TiO_2:SnO_2 heterostructure induced by photocatalysis (P), electrocatalysis (E), and photoelectrocatalysis (PE) sources. The reactions were made in 0.5M Na_2CO_3 at pH 12 for 1 hour. Priorly to the reactions, N_2 and methane gas were purged. Chronoamperometric measurements at 1.3 V for electron reactions, a 100 W halogen lamp source for photon reactions, and both chronoamperometric measurements at 1.3 V and a 100 W halogen lamp source were applied for photoelectron reactions. All trials were made in a discontinuous mode under reservoir recirculation. More details are found in the flow cell configuration section.

radical ($\bullet CH_3$), which reacts with an additional water molecule (H_2O), forming methanol (CH_3OH) [11]. When just excited by an electron source, as-synthesized SnO_2-rutile electrodes exhibited a better performance in comparison to the commercial TiO_2-anatase and a slightly better performance than as-synthesized TiO_2:SnO_2 heterojunction electrodes. This finding can be addressed with the strong SnO_2 electrocatalytic activity since it possesses good electrical conductivity, which helps in facilitating the flow of electrons during electrochemical reactions, and the catalytic activation through photoactivation is not significant. Under an electron source, commercial TiO_2-anatase exhibited better performance when compared to its production under just photon irradiation, indicating a possible limitation of efficiency by the recombination rate of the e^-/h^+ pairs. When excited by a photoelectron source, as-synthesized TiO_2:SnO_2 heterojunction electrodes exhibited superior performance compared to the as-synthesized SnO_2-rutile and commercial TiO_2-anatase. As-synthesized TiO_2:SnO_2 heterojunction electrodes under photoelectron excitation source exhibited higher methanol and acid acetic production of 30 and 8 $\mu mol.cm^{-2}.h^{-1}$, respectively, among all catalysts and conditions studied. This finding may be attributed to the heterojunction that enables a more effortless transfer between bands, facilitating the separation of the generated e^-/h^+ pairs when under UV-Vis irradiation. Ultimately, the photoelectrocatalytic experiments denote the importance of electron drainage (i.e., the transfer of electrons from the photocathode to the oxidant), improved by the TiO_2:SnO_2 heterojunction catalyst when compared to their individual material alone. The electrons accumulated in SnO_2-rutile could be transferred to TiO_2-anatase in the circuit, increasing of oxidative potential and therefore the total catalytic activity. Commercial TiO_2-anatase and the as-synthesized TiO_2:SnO_2 heterojunction showed equivalent behavior when excited by the different sources, demonstrating that the effects are related to the TiO_2-anatase photocatalytic properties since its surface area is ~50 times lower than SnO_2-rutile. In addition, the formed products did not alter among all catalysts studied, suggesting that the methane activation is taking place over the TiO_2-anatase surface, where we believe the oxidative sites are concentrated. Acetic acid production followed the behavior of methanol production because the accumulation of intermediates and products formed during the reaction may promote the dimerization of methane molecules, thus enabling the formation of both C1 and C2 compounds; the reactions are performed in an inflow and sealed system to stimulate acetic acid formation following methanol production. This is because the chemical pathway to form acetic acid goes through a methanol intermediate step, so a sealed system helps by maintaining a constant environment around the electrodes.

4. Conclusion

In this study, we synthesized and characterized an as-synthesized TiO_2:SnO_2 heterojunction as a model catalyst for controlled photoelectrochemical methane oxidation, prepared from pre-formed nanoparticles via a hydrothermal method. As-synthesized TiO_2:SnO_2 heterostructure electrodes excited by a photoelectron source exhibited superior performance for methanol (30 $\mu mol.cm^{-2}.h^{-1}$) and acetic acid (8 $\mu mol.cm^{-2}.h^{-1}$) production when compared to their individual materials alone (i.e., TiO_2-anatase and SnO_2-rutile). The superior production could be attributed to the heterojunction mechanism between TiO_2-anatase and SnO_2-rutile materials that enables a more effortless transfer between bands, facilitating the separation of the generated electron-hole (e^-/h^+), liable for producing reactive oxygens (e.g., $\bullet OH$), which are essential to driving methane oxidation conversion by the C–H bond cleavage. Our insights show that the e^-/h^+ separation process, probed by this model catalyst, can increase methane conversion; however, it depends on proper electron drainage (to a related oxidation reaction or in the photoelectrochemical circuit). The electron concentration in one phase may increase its transference in the electrochemical circuit in a synergic way with irradiation. The product selectivity is not altered from the commercial TiO_2-anatase to the as-synthesized TiO_2:SnO_2 heterostructure, showing that this factor is related to the TiO_2-anatase catalyst's nature. The results can support new research about how heterostructure design can impact with the performance of photoelectrocatalysts and stimulate the development of novel materials/combinations for various other applications, including water splitting, CO_2 reduction, and pollutant degradation.

Funding

The authors gratefully acknowledge the financial support given by FAPESP (2020/09628–6, 2021/13065–0, 2018/01258–5, 2019/10689–2, 2022/10255–5, 2019/21496-0, and 2022/05149-1) and CAPES (Finance Code 001).

CRediT authorship contribution statement

Ricardo Marques e Silva: Conceptualization, Methodology, Investigation, Data curation, Writing - original draft, Writing - Reviewing and Editing. **Fernanda de Lourdes Souza:** Methodology, Investigation, Reviewing. **Eduardo Dias:** Methodology, Data curation, Writing. **Gelson Tiago dos Santos Tavares da Silva:** Methodology, Data curation, Writing. **Florymar Escalona DuráN:** Methodology, Investigation. **Arjun Rego:** Writing - Reviewing and Editing. **Drew Higgins:** Reviewing and Editing. **Caue Ribeiro de Oliveira:** Funding acquisition, Supervision, Conceptualization, Reviewing and Editing.

Declaration of Competing Interest

The authors declare that they have no known competing financial interests or personal relationships that could have appeared to influence the work reported in this paper.

Data Availability

Data will be made available on request.

Acknowledgments

The authors thank Dr. Jéssica Ariane de Oliveira for her valuable contribution to the development and design of the reactor utilized in this project, supported by FAPESP (2019/21496-0 and 2022/05149-1). We thank the Structural Characterization Laboratory (LCE) at the Federal University of São Carlos for the electron microscopy analyses.

Appendix A. Supporting information

Supplementary data associated with this article can be found in the online version at doi:10.1016/j.jallcom.2023.172090.

REFERENCES

[1] K. Huang, J.B. Miller, G.W. Huber, J.A. Dumesic, C.T. Maravelias, A General Framework for the Evaluation of Direct Nonoxidative Methane Conversion Strategies, Joule 2 (2018) 349–365, https://doi.org/10.1016/j.joule.2018.01.001.

[2] W. Li, D. He, G. Hu, X. Li, G. Banerjee, J. Li, S.H. Lee, Q. Dong, T. Gao, G. W. Brudvig, M.M. Waegele, D.E. Jiang, D. Wang, Selective CO Production by Photoelectrochemical Methane Oxidation on TiO2, ACS Cent. Sci. 4 (2018) 631–637, https://doi.org/10.1021/acscentsci.8b00130.

[3] M.J. Boyd, A.A. Latimer, C.F. Dickens, A.C. Nielander, C. Hahn, J.K. Nrskov, D. C. Higgins, T.F. Jaramillo, Electro-Oxidation of Methane on Platinum under Ambient Conditions, ACS Catal. 9 (2019) 7578–7587, https://doi.org/10.1021/acscatal.9b01207.

[4] M.S.A. Sher Shah, C. Oh, H. Park, Y.J. Hwang, M. Ma, J.H. Park, Catalytic Oxidation of Methane to Oxygenated Products: Recent Advancements and Prospects for Electrocatalytic and Photocatalytic Conversion at Low Temperatures, Adv. Sci. 7 (2020), https://doi.org/10.1002/advs.202001946.

[5] A.M. Ismail, G.F. Samu, H.C. Nguyën, E. Csapó, N. López, C. Janáky, Au/Pb Interface Allows the Methane Formation Pathway in Carbon Dioxide Electroreduction, ACS Catal. 10 (2020) 5681–5690, https://doi.org/10.1021/acscatal.0c00749.

[6] M.M. Wang, Y.X. Zhao, X.L. Ding, W. Li, S.G. He, Methane activation by heteronuclear diatomic AuRh+ cation: Comparison with homonuclear Au2+ and Rh2+, Phys. Chem. Chem. Phys. 22 (2020) 6231–6238, https://doi.org/10.1039/c9cp05699h.

[7] I. Barba-Nieto, N. Gómez-Cerezo, A. Kubacka, M. Fernández-García, Oxide-based composites: Applications in thermo-photocatalysis, Catal. Sci. Technol. 11 (2021) 6904–6930, https://doi.org/10.1039/d1cy01067k.

[8] A. Chuvilin, E. Bichoutskaia, M.C. Gimenez-Lopez, T.W. Chamberlain, G.A. Rance, N. Kuganathan, J. Biskupek, U. Kaiser, A.N. Khlobystov, Self-assembly of a sulphur-terminated graphene nanoribbon within a single-walled carbon nanotube, Nat. Mater. 10 (2011) 687–692, https://doi.org/10.1038/nmat3082.

[9] M. Zhou, H. Wang, Optimally Selecting Photo- and Electrocatalysis to Facilitate CH4 Activation on TiO2 (110) Surface: Localized Photoexcitation versus Global Electric-Field Polarization, JACS Au 2 (2022) 188–196, https://doi.org/10.1021/jacsau.1c00466.

[10] L. Xie, T. Du, J. Wang, Y. Ma, Y. Ni, Z. Liu, L. Zhang, C. Yang, J. Wang, Recent advances on heterojunction-based photocatalysts for the degradation of persistent organic pollutants, Chem. Eng. J. 426 (2021), https://doi.org/10.1016/j.cej.2021.130617.

[11] J. Liu, Y. Zhang, Z. Huang, Z. Bai, Y. Gao, Photoelectrocatalytic Oxidation of Methane into Methanol over ZnO Nanowire Arrays Decorated with Plasmonic Au Nanoparticles, Nano 14 (2019), https://doi.org/10.1142/S1793292019500176.

[12] C. Ribeiro, E. Longo, E.R. Leite, Tailoring of heterostructures in a SnO2-TiO2 system by the oriented attachment mechanism, Appl. Phys. Lett. 91 (2007), https://doi.org/10.1063/1.2779932.

[13] V.R. De Mendonça, O.F. Lopes, R.P. Fregonesi, T.R. Giraldi, C. Ribeiro, TiO2-SnO2 heterostructures applied to dye photodegradation: The relationship between variables of synthesis and photocatalytic performance, Appl. Surf. Sci. 298 (2014) 182–191, https://doi.org/10.1016/j.apsusc.2014.01.157.

[14] R.B. Rajput, S.N. Jamble, R.B. Kale, A review on TiO2/SnO2 heterostructures as a photocatalyst for the degradation of dyes and organic pollutants, J. Environ. Manag. 307 (2022), https://doi.org/10.1016/j.jenvman.2022.114533.

[15] J.A. Torres, G.T.S.T. Da Silva, F. Barbosa de Freitas Silva, C. Ribeiro, Experimental Evidence of CO_2 Photoreduction Activity of SnO2 Nanoparticles, ChemPhysChem 21 (2020) 2392–2396, https://doi.org/10.1002/cphc.202000786.

[16] D.L. Wood, J. Tauc, Weak absorption tails in amorphous semiconductors, Phys. Rev. B 5 (1972) 3144–3151, https://doi.org/10.1103/PhysRevB.5.3144.

[17] X. Zhu, S.S. Jan, F. Zan, Y. Wang, H. Xia, Hierarchically branched TiO2@SnO2 nanofibers as high performance anodes for lithium-ion batteries, Mater. Res Bull. 96 (2017) 405–412, https://doi.org/10.1016/j.materresbull.2017.03.068.

[18] S. Yang, Z. Wu, L.P. Huang, B. Zhou, M. Lei, L. Sun, Q. Tian, J. Pan, W. Wu, H. Zhang, Significantly enhanced dye removal performance of hollow tin oxide nanoparticles via carbon coating in dark environment and study of its mechanism, Nanoscale Res Lett. 9 (2014), https://doi.org/10.1186/1556-276X-9-442.

[19] H. Wang, J. Liu, X. Xiao, H. Meng, J. Wu, C. Guo, M. Zheng, X. Wang, S. Guo, B. Jiang, Engineering of SnO2/TiO2 heterojunction compact interface with efficient charge transfer pathway for photocatalytic hydrogen evolution, Chin. Chem. Lett. (2022), https://doi.org/10.1016/j.cclet.2022.01.018.

[20] M. Thommes, K. Kaneko, A.V. Neimark, J.P. Olivier, F. Rodriguez-Reinoso, J. Rouquerol, K.S.W. Sing, Physisorption of gases, with special reference to the evaluation of surface area and pore size distribution (IUPAC Technical Report), Pure Appl. Chem. 87 (2015) 1051–1069, https://doi.org/10.1515/pac-2014-1117.

[21] F. Silva, G. da Silva, J. Torres, C. Ribeiro, Tuning the Photocatalytic Activity of Tin Oxide Through Mechanical Surface Activation, J. Braz. Chem. Soc. (2022), https://doi.org/10.21577/0103-5053.20220009.

[22] V.R. de Mendonça, W. Avansi, R. Arenal, C. Ribeiro, A building blocks strategy for preparing photocatalytically active anatase TiO2/rutile SnO2 heterostructures by hydrothermal annealing, J. Colloid Interface Sci. 505 (2017) 454–459, https://doi.org/10.1016/j.jcis.2017.06.024.

[23] L. Chetibi, T. Busko, N.P. Kulish, D. Hamana, S. Chaieb, S. Achour, Photoluminescence properties of TiO2 nanofibers, J. Nanopart. Res. 19 (2017), https://doi.org/10.1007/s11051-017-3822-x.

[24] B. Anitha, M.A. Khadar, Anatase-rutile phase transformation and photocatalysis in peroxide gel route prepared TiO2 nanocrystals: Role of defect states, Solid State Sci. 108 (2020), https://doi.org/10.1016/j.solidstatesciences.2020.106392.

[25] S.M. Deshmukh, S.S. Patil, S.B. Babar, S. Alshehri, M.M. Ghoneim, A.M. Tamboli, N.H. Lam, N.T.N. Truong, C.D. Kim, M.S. Tamboli, S.M. Khetre, S.R. Bamane, TiO2–SnO2 Nanocomposites for Photocatalytic Environmental Remediation under UV-Light, Met. (Basel) 12 (2022), https://doi.org/10.3390/met12050733.